Temperature measurement

The gas-kinetic temperature was estimated by measuring the excitation temperature. The magnitude of the two temperature are similar. [1]

$$T_{rot} < T_D \approx T_{gas} \approx T_{exc} < T_{ion} < T_e$$

As the single-particle measurements were conducted in a dry ICP, the temperature was measured using dried aerosols of Fe standard solution. The ICP operating parameters were identical to the ones used for single-particle measurements (Table 1). 1000-ppm Fe standard solution was nebulized using a concentric nebulizer (TR-30-C2, Meinhard Glass Products, USA) at sample uptake rate of 0.4 mL/min. Large aerosols were removed by a Scott-type double-pass spray chamber. The filtered aerosols then passed through a heating chamber-condenser assembly: a glass tube (ID = 22 mm, length = 250 mm) wrapped with a heating tape and a U-shaped cold trap (ID = 22 mm, length = 150 mm) immersed in an ice-water bath. The temperature at the outlet of the heating tube was measured to be approximately 150 °C using a thermocouple. The aerosols were assumed to have been completely evaporated in the heating tube. The water vapor was condensed in the U-shaped cold trap to remove the water vapor from the Ar stream. The saturated water vapor density is 4.85 g/m^3 at the freezing point which is assumed to be insignificant on ICP excitation conditions.

The emission intensity of four Fe emission lines, 371.99, 373.49, 374.56 and 375.82 nm, were measured for the construction of the Boltzmann plot. The excitation energies, statistical weights and transition probabilities of these lines are listed in Table S1. The ICP excitation temperature was determined from the Boltzmann plot of ln(Iλ/gA) versus the excitation energies of the emission lines[2]. The excitation temperature is equal to -5040/slope. The measurement was repeated across the radial position of -1.5 to +1.5 mm in steps of 0.375 mm at observation positions of 8.5 mm and 19.5 mm ALC. The radial temperature profiles are shown in Figure S1. The vertical temperature profile of the ICP central channel from 6.5 to 18.5 mm ALC has also been measured in the same way (Figure S2). The excitation temperature generally increases with observation position up to 16.5 mm ALC and rolls off at 18.5 mm. The trend is consistent with the profile in the literatures.[3–7]

Characterization of the sheath gas device

The dimension (outer diameter) of the concentric sheath-gas and central-gas flows were determined by measuring the laser-scattering images of aerosols of water in the gas flows. Water aerosols were used instead of Yb_2O_3 particles because a steady stream of the water aerosols is readily generated using a concentric nebulizer / spray chamber. The aerosols are also relative large (diameter of a few micrometers) and high in number density ($10^7/cm^3$).[8] The scattered intensity is relatively high and shape and size of the gas flows are readily observed and recorded using a smart phone camera.

An additional advantage of using water aerosols as a surrogate of the Yb_2O_3 particles is that the Stokes number of both particles is well below 1 at volumetric gas flow rate of 0.4 – 1.0 L/min, which corresponds to gas velocity of 0.2 – 0.6 m/s in the sheath gas device. The Stokes number is given by Equation 2 below.

$$S = \frac{\rho_p d_p^2 u}{18 \mu_g L} \qquad (2)$$

where

ρ_p = density of the particle (kg/m^3),

d_p = particle diameter (m),

μ_g = dynamic viscosity of the fluid (Pa s)

u = fluid velocity (m/s)

L = characteristic dimension of the obstacle (m)

For example, the Stokes number of a 2-µm Yb_2O_3 and a 10-µm water droplet are 0.009 and 0.025 at gas flow rate of 1 L/min. The small Stokes number signifies that both particles are effectively entrained in the gas stream.

A concentric nebulizer (TR-30-C2, Meinhard Glass Products, USA) and a Scott-type double-pass spray chamber were used to generate the water aerosols. The water uptake rate was 0.4 mL/min. The carrier gas flowrate was 0.43 to 1.00 L/min. A cylindrical lens (focal length = 20 cm) was used to shape a circular frequency-doubled Nd:YAG laser beam into a rectangular beam of dimension of 2 mm × 30 mm. The laser beam intercepts the Ar flow 5 mm below the exit of the spray chamber to

visualize the cross-section of the aerosol distribution, which is taken as the cross-sectional dimension of the Ar flow.

Figure S3a shows the laser-scattering image of the cross-section of the aerosol flow at the exit of the spray chamber. The Ar carrier gas flow rate was 1.0 L/min. The cross-section was embryo-shaped rather than circular. The void of aerosols in the flow (and thus the dimmed laser scattering) is due to more severe inertial deposition of the aerosols on the chamber wall and gravitational settling of aerosols of the dead volume at the back of the spray chamber (located at the top-right corner in Figure S3). Figure S3b shows the laser-scattering image of the cross-section at reduced Ar carrier gas flow rate of 0.86 L/min. The effect of Ar flow rate on the dimension and pattern of the cross-section appears to be insignificant.

Figure S4a shows the laser-scattering image of the cross-section of the aerosol flow after the Ar flow passed through the sheath gas device and the injector tube of the ICP torch. The aerosols from the spray chamber were introduced to the central tube of the sheath gas device. The Ar flow rate was 1.00 L/min. No sheath gas flow was used. The embryo-shaped cross section was preserved over the additional path of the sheath gas device and the injector tube, indicating a well-preserved laminar flow through the devices. In contrast to the relatively constant dimension of the gas flow at the exit of the spray chamber (Figure S3a and b), the cross-sectional dimension of the central gas flow decreases as the central gas flow rate decreases (Figure S4b). The central-gas and sheath-gas flow rates were 0.86 L/min and 0.14 L/min, respectively, to maintain a constant total flow rate of 1.00 L/min. The dimension of the gas flow can be estimated readily by measuring the largest diameter of the cross-section. Figure S5 shows a plot of the outer diameter of the central gas flow versus the central gas flow rate. The diameter increases linearly with the gas flow rate.

Figure S6 shows the laser-scattering image of the sheath gas flow at the exit of the injector of the ICP torch. The Ar carrier gas was connected to the sheath gas inlet of the sheath gas device so that the water aerosols were entrained in the sheath gas flow. The sheath gas flow rate was 0.71 L/min and the central gas flow rate was 0.29 L/min to give a total flow rate of 1.00 L/min. As the sheath gas flow at the entrance of the sheath gas device is perpendicular to the central tube of the device, the central tube induces disturbance to the sheath gas flow. The gas flow is expected to be an oscillating Karman vortex street wake.[9] Although the sheath gas flow is not strictly a laminar flow, the dimension of the cross-section of the flow can still be determined from the laser-scattering image of the entrained water aerosols because the Stokes number is much smaller than 1 and the aerosols are entrained in the flow effectively. The inner and outer diameter of the cross section of the flow

were determined by fitting a circle to the laser-scattering image using the image processing software ImageJ v1.52i.

In addition to the outer diameter of the cross section of the central gas flow, Figure S5 shows the plot of the inner diameter of the sheath gas flow *versus* the central gas flow rate. The inner diameter also increases linearly with central gas flow rate. It is interesting to note that the plots of the inner diameter of the sheath gas flow and the outer diameter of central gas flows overlap, indicating that the aerosols are confined within the flows with relatively sharp boundary between the flows. At gas flow rate of 0.5 L/min for both gas flows, which is used in this study, the two diameters are approximately the same.

Experimental calibration curve of I_1 versus I_2

The base of particle size determination by SP-ICP-MS and SP-ICP-AES is that a calibration curve of measured intensity *versus* particle mass exists and the curve is a monotonic increasing function, *i.e.*, any measured intensity corresponds to one particle mass only. The practically identical calibration curves of simulated I_2 versus particle diameter for the outer and center portion of the ICP central channel (Figure 8) indicates that such calibration is feasible for SP-ICP-AES measurement at high observation positions. Furthermore, the similar distributions of experimental I_2 for the two regions of the ICP central channel (Figure 2a) and I_2 over the entire central channel in the absence of a sheath flow (Figure 4a) indicate that the relationship between SP-ICP-AES intensity at 19.5 mm ALC and particle size is robust, independent of the radial location of the particles in the central channel. In other words, in the absence of standard Yb_2O_3 for size calibration, SP-ICP-AES intensity measured at high observation position (e.g., I_2 measured at 19.5 mm ALC) can be used as a surrogate of particle mass for the preparation of calibration curve of the measured intensity at lower observation position for the same population of Yb_2O_3 particles. Such calibration is instructive in understanding the potential pitfalls of measurement of SP-ICP-AES intensity at low observation positions for particle size determination because of the effects of the radial location of the particles on SP-ICPAES intensity.

Two calibration curves of I_1 *versus* I_2 (Figure S7) are prepared from the data of the DVP-SP-ICP-AES measurement in Figure 1. In the first calibration curve (round red dots), the distributions of all I_1 and I_2 in Figure 1c, irrespective of the radial location of the particles in the ICP central channel, are divided separately into the same number of equal portions. (10 portions in this case). The average intensity in each portion of I_1 is plotted *against* the corresponding portion of I_2, i.e., the first portion of I_1 (the smallest I_1) is correlated with the first portion of I_2 (the smallest I_2), and so on. The assumption of such calibration is that the measured intensity at all observation positions (both I_1 and I_2 in this case) is proportional to particle mass. A relatively linear calibration curve of I_1 vs I_2 is obtained (Figure S7). It appears that calibration is successful even at the low observation position (8.5 mm ALC in this case) where DOV is very small and is negligible for large particles at the center of the ICP central channel. The calibration curve, however, is incorrect because there are in fact two distinct distributions of I_1 for the two regions of the ICP central channel (Figure 2b). The dissimilar distributions suggest that the same measured intensity could originate from particles of significantly different mass. The second calibration curve (square black dots) in Figure S7 demonstrate such characteristics, *i.e.*, a measured intensity may not correspond to one particle mass only. The second calibration curve is constructed by dividing I_2 into 10 equal portions as before. However, for each

pair of I_1 and I_2 in a double peak, I_1 is assigned to a portion corresponding to the portion of I_2, irrespective of the magnitude of I_1. The average I_1 in each portion is calculated for the construction of the calibration curves. In other words, the average "linked I_1" is plotted against the average I_2 in the corresponding portion to give the second calibration curve in Figure S7 (square black dots). The use of linked I_1 gives proper calibration because the measured I_1 corresponding to the particle mass (as represented by I_2) is used. The concave calibration curve shows that determination of particle mass based on measured SP-ICP intensity can be erroneous at low observation position where the particles have just reached the boiling point and start to vaporize. The problem can be identified by using a set of monodisperse standard particles to construct a calibration curve which would result in a similar non-monotonic concave calibration curve. The problem, however, will not be identified when a set of solution standards or a single particle standard (one-point calibration) is used in the calibration.

Adjustment of the scale of the simulated intensity

The emission intensity from a particle can be calculated using the following equation.[10]

$$I = \Phi\left(\frac{hcgAN}{4\pi\lambda Z}\right) exp\left(\frac{-E}{kT}\right)$$

where

Φ = the solid angle
h = Planck constant
c = speed of light
g = the statistical weight
A = transition probability
N = total population
λ = emission wavelength
Z = partition function
E = excitation energy
k = Boltzmann constant
T = excitation temperature

The intensity of a 200-nm Yb_2O_3 particle (number of free Yb ions in the ICP = 10^5) is in the order of 10^{-10} W. To convert the emission intensity (W) into voltage, corresponding to the output of the PMT, the overall light transmission efficiency of the focusing lens, optical fiber bundles, and the spectrometer, as well as the conversion factor of light intensity into current of the PMT and the amplification of the pre-amplifier must be considered. The light transmission efficiency was calculated based on the solid angle of light admittance of the fiber bundle and the transmission efficiency from the fiber to the rectangular entrance slit of the monochromator. The estimated magnitude of the light transmission efficiency and the conversion factor of the PMT are given in Table S2. The overall conversion factor of 10^7 was used to convert the calculated emission intensity into output voltage of the pre-amplifier for direct comparison with the experimentally measured voltage (Figures 1 and 7).

References

1 A. Montaser and D. W. Golightly, *Inductively coupled plasmas in analytical atomic spectrometry*, VCH Publishers, 1992, p. 392.

2 *Inductively coupled plasma spectrometry and its applications*, ed. S. J. Hill, Sheffield Academic Press, CRC Press, London, Boca Raton, FL, 1999, p. 49.

3 M. Huang, S. A. Lehn, E. J. Andrews and G. M. Hieftje, *Spectrochimica Acta Part B: Atomic Spectroscopy*, 1997, **52**, 1173–1193.

4 M. Huang, D. S. Hanselman, P. Yang and G. M. Hieftje, *Spectrochimica Acta Part B: Atomic Spectroscopy*, 1992, **47**, 765–785.

5 D. S. Hanselman, N. N. Sesi, M. Huang and G. M. Hieftje, *Spectrochimica Acta Part B: Atomic Spectroscopy*, 1994, **49**, 495–526.

6 M. Ohata and N. Furuta, *Journal of Analytical Atomic Spectrometry*, 1997, **12**, 341–347.

7 N. Furuta, *Spectrochimica Acta Part B: Atomic Spectroscopy*, 1985, **40**, 1013–1022.

8 J. W. Olesik, *Appl. Spectrosc.*, 1997, **51**, 158A-175A.

9 B. R. Munson, T. H. Okiishi, W. W. Huebsch and A. P. Rothmayer, *Fundamentals of fluid mechanics*, John Wiley & Sons, Inc, Hoboken, NJ, 7th edition., 2013, p. 520.

10 *Inductively coupled plasma spectrometry and its applications*, ed. S. J. Hill, Sheffield Academic Press, CRC Press, London, Boca Raton, FL, 1999, p. 39.

Table S1. Excitation energy, statistical weight, and transition probability of the Fe emission lines.

Wavelength, nm	Excitation energy E_{exc} (cm^{-1})	Statistical weight g	Transition probability A (10^8 s^{-1})
371.99	26875	11	0.162
373.49	33695	11	0.902
374.56	27395	7	0.115
375.82	34329	7	0.634

Table S2. Conversion factors of light intensity from the units of Watt to Volt.

Conversion Factors	Magnitude
Light transmission efficiency	10^{-4}
PMT current amplification	10^6 A/W
Pre-amplifier	10^5 V/A
Overall	10^7 V/W

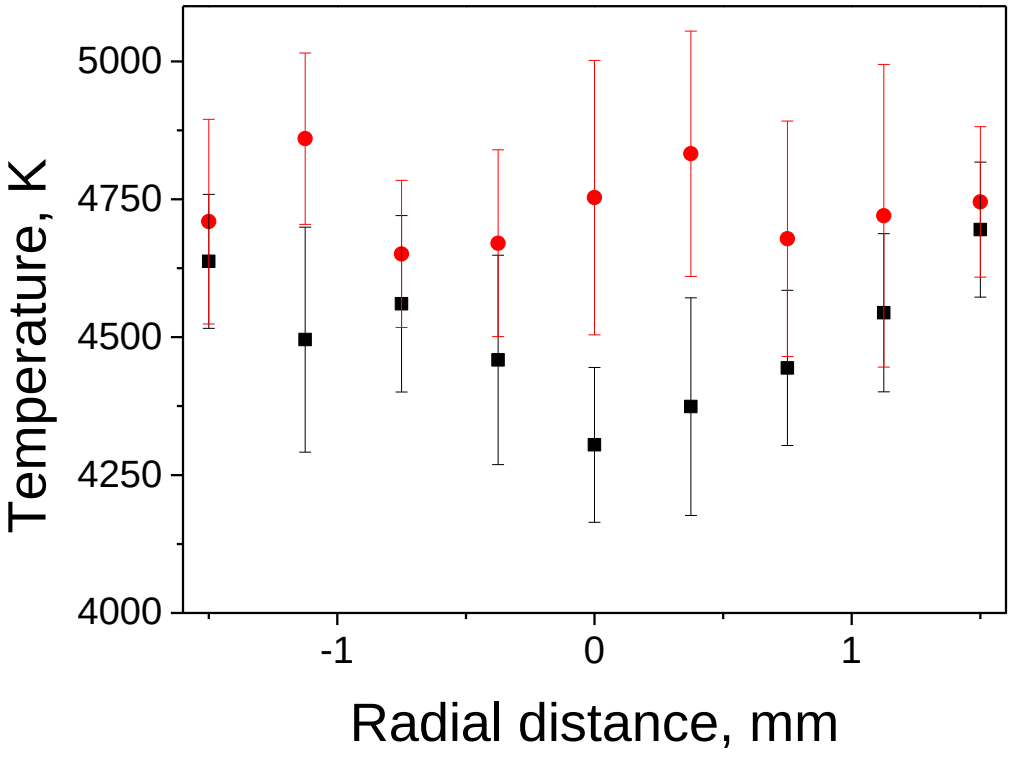

Figure S1. Radial excitation temperature profiles at 8.5 mm (■) and 19.5 mm ALC (●).

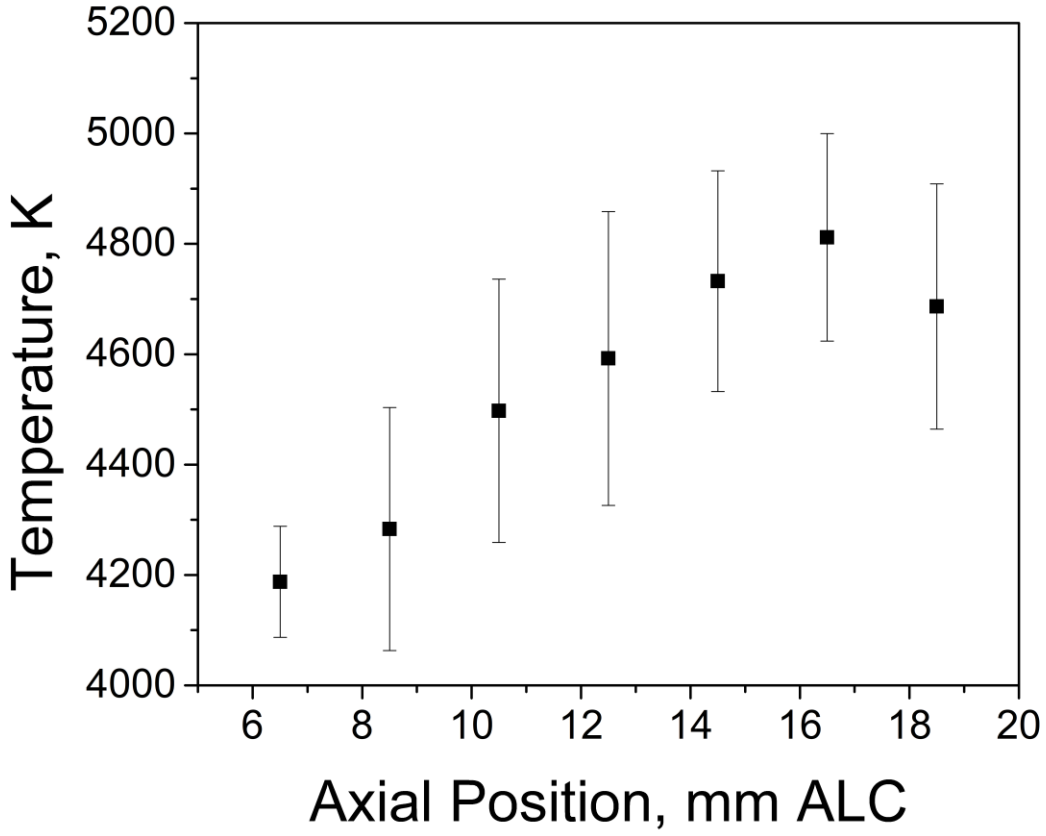

Figure S2. Axial excitation temperature profile at the center of central channel.

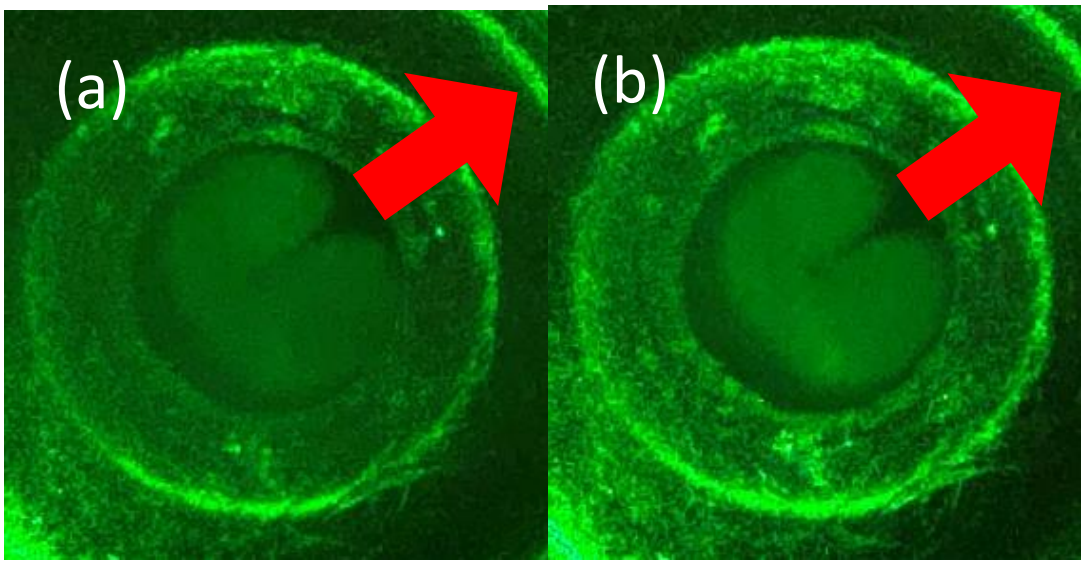

Figure S3. Cross-section of the aerosol flow at the exit of spray chamber. Nebulizing gas flowrate (a) 1.00 L/min and (b) 0.86 L/min. The red arrow indicates orientation of the long axis of the spray chamber. The arrow points to the location of the dead volume at the end of the spray chamber.

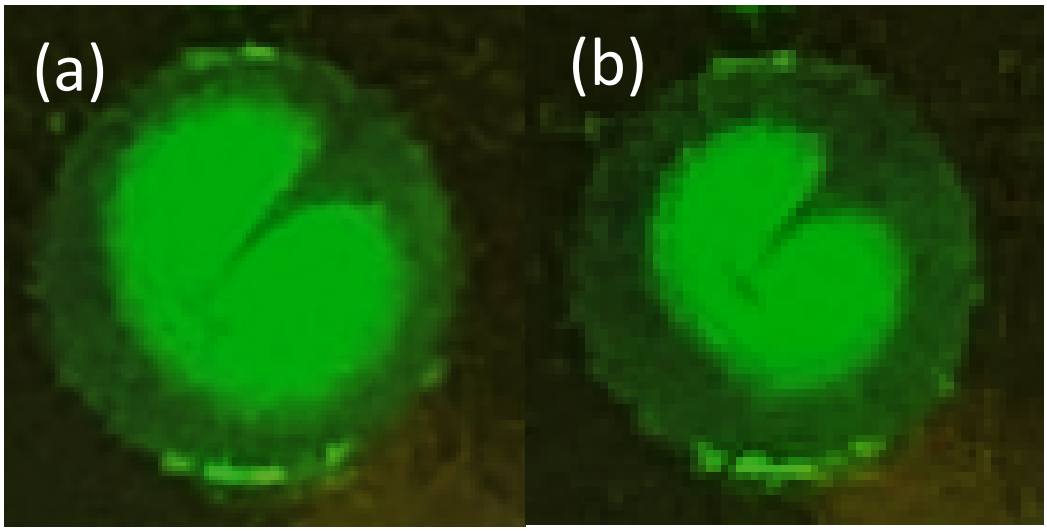

Figure S4. Cross-section of the aerosol flow at the exit of the 1.5-mm injector tube of the ICP torch. The aerosols were entrained in the central gas flow of the sheath gas device at flow rate of (a) 1.00 L/min and (b) 0.86 L/min. The total gas flow rate was 1.0 L/min.

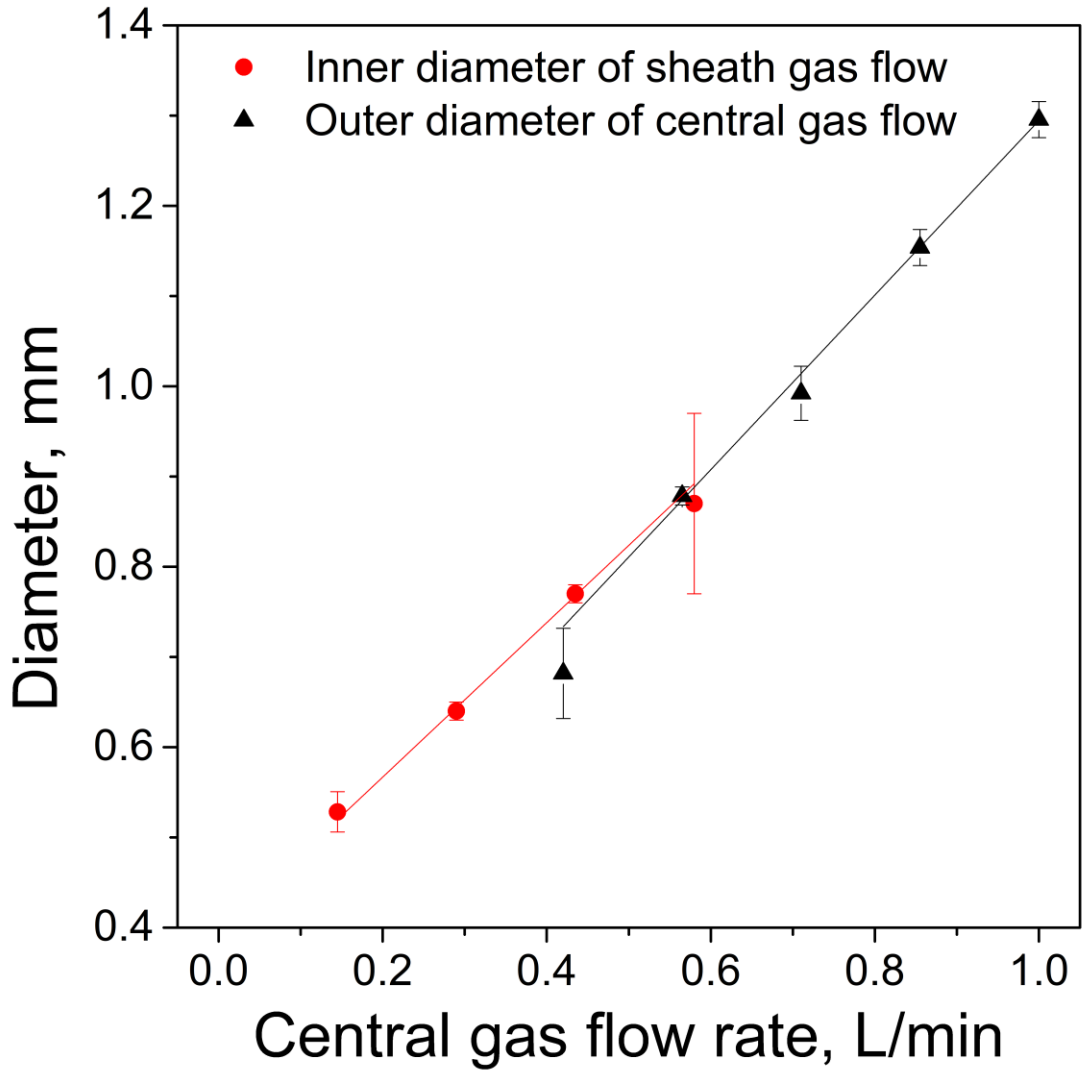

Figure S5. Dimension of the sheath (●) and central (▲) gas flows at the exit of the injector of the ICP torch versus central gas flow rate. The total gas flow rate was 1.0 L/min.

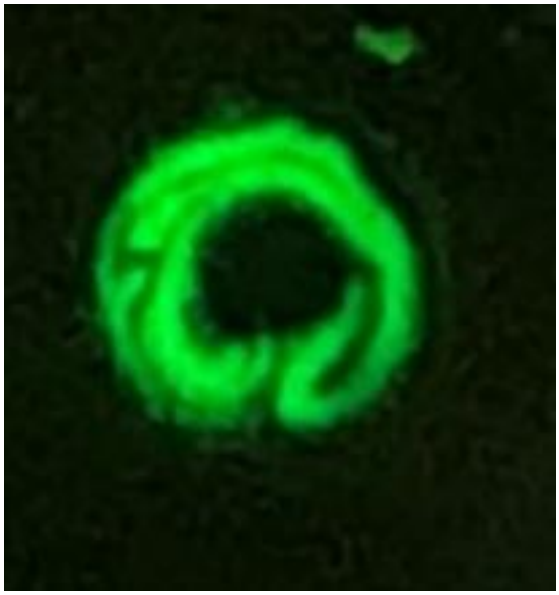

Figure S6. Cross-section of the aerosol flow in the sheath gas steam at the exit of the 1.5-mm injector tube of the ICP torch. The sheath gas flow rate of the sheath gas device was 0.71 L/min. The total gas flow rate was 1.0 L/min.

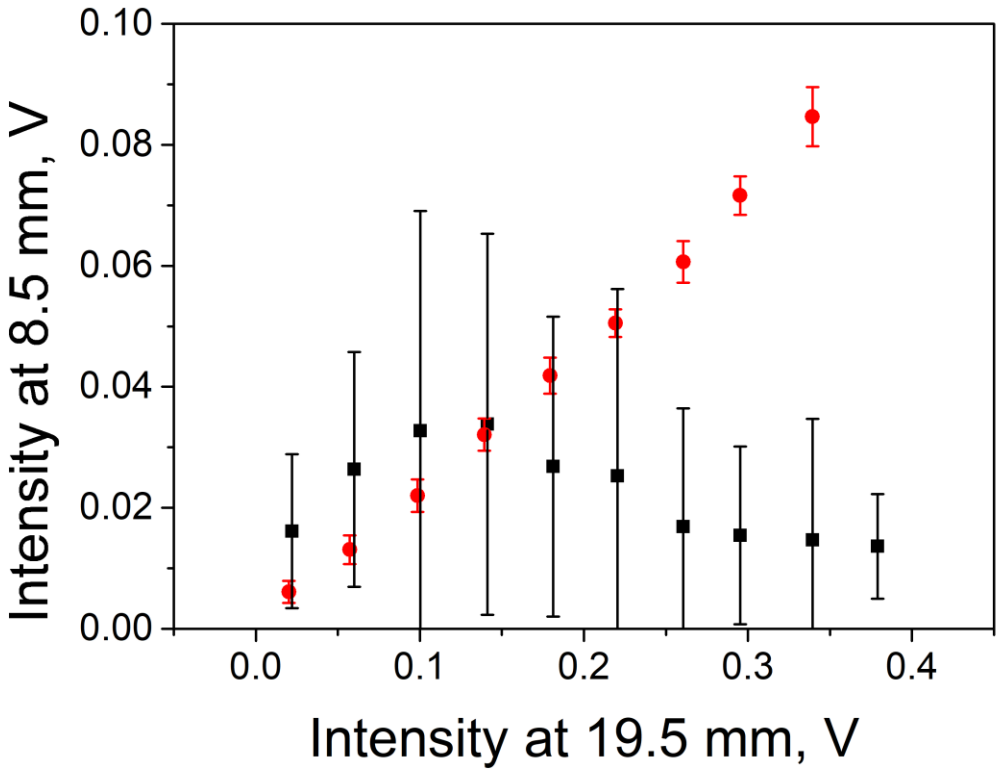

Figure S7. Calibration plot of delinked (●) and linked (■) intensity of Yb_2O_3 at observation position of 8.5 mm ALC vs intensity at 19.5 mm ALC.